

# Modelling the influence of the fibre structure on the structural behaviour of flowable fibre-reinforced concrete



E.V. Sarmiento<sup>a,\*</sup>, M.A.N. Hendriks<sup>a,b</sup>, M.R. Geiker<sup>a</sup>, T. Kanstad<sup>a</sup>

<sup>a</sup> Department of Structural Engineering, Norwegian University of Science and Technology (NTNU), Trondheim, Norway

<sup>b</sup> Faculty of Civil Engineering and Geosciences, Department of Structural Engineering, Delft University of Technology, Delft, The Netherlands

## ARTICLE INFO

### Article history:

Received 26 September 2015

Revised 26 April 2016

Accepted 31 May 2016

### Keywords:

Fibre reinforced concrete  
Inhomogeneity of the fibre structure  
Fibre orientation tensor  
Fibre volume fraction  
Nonlinear finite element modelling

## ABSTRACT

This paper presents a modelling approach for fibre-reinforced concrete elements in which the fibre structure is taken into account in simulating the mechanical behaviour. The fibre structure is discretized in volumes and two fibre parameters are defined for each discrete volume: the dominant fibre orientation and the fibre volume fraction. These parameters are incorporated in a numerical model that uses a single-phase material definition dependent on the fibre parameters. The first part of this paper describes the methodology and constitutive modelling. The second part addresses the simulation of two beams that exhibited large differences in bending because of uneven fibre distribution. Data on the fibre structure was obtained using Computed Tomography scanning. The modelling approach captured the large difference in the flexural response of the two beams and provided an adequate prediction of the location and propagation of the critical cracks.

© 2016 Elsevier Ltd. All rights reserved.

## 1. Introduction

Predicting the overall mechanical behaviour of a fibre-reinforced concrete (FRC) element usually requires the characterization of the post-cracking behaviour of the FRC. This is often determined either directly, in direct tension tests (e.g., RILEM [41]), or indirectly by performing inverse analysis of bending tests, splitting tests, or other indirect tension tests [1–5]. Inverse analysis of the test results makes it possible to determine the material tensile behaviour considering a certain stress-strain or stress-crack width relationship. Bi-, tri- and poly-linear functions are usually proposed in the literature to describe the post-cracking behaviour of FRC [4,6–14]. Several technical recommendations [15–18] also provide simplified formulations of the constitutive behaviour of FRC based on bending tests, which facilitate the material characterization for design purposes.

The post-cracking behaviour of FRC in a structural element, especially if it is flowable or self-compacting FRC, can differ from the post-cracking behaviour of a test specimen. The rheological properties, the casting procedure, and the structural geometry can lead to an uneven fibre structure in the element, meaning inhomogeneity of the fibre volume over the length or depth of the element and a preferred alignment of the fibres [19–24]. In

such cases, modelling the FRC as if it were a homogeneous material can lead to inaccurate results.

In an attempt to take into account its fibre structure, FRC can be modelled as a two-phase material [25–27], where the concrete matrix is described as a homogeneous material, while the fibres are treated explicitly as discrete entities. This approach has the advantage of directly including the effect of fibre location and orientation, but requires a definition of the concrete matrix model, the fibre model, and the interface model for the fibre-matrix bond response. This response is often based on results from pull-out tests of single fibres and/or analytical expressions that include effects such as the fibre embedded length, fibre inclination, or the anchorage of the fibre end [28,29]. It is commonly assumed that fibres do not interact with neighbouring fibres, but when a large fibre dosage is used, failure mechanisms can be interactive, creating a collective failure that cannot be captured by describing the failures of individual fibres [28,30].

The current paper presents a modelling approach for analysing FRC structural elements in which the fibre structure is modelled by assuming volume-wise constant material properties. Since the material cannot be assumed to be homogeneous on the scale of the structural element, a spatial discretization of the element is defined within which the material can be considered homogeneous. The process consists of (see Fig. 1): (i) obtaining the fibre structure, (ii) discretizing the structural element in volumes, (iii) determining the fibre structure properties within each discrete

\* Corresponding author.

E-mail address: [elena.sarmiento@ntnu.no](mailto:elena.sarmiento@ntnu.no) (E.V. Sarmiento).

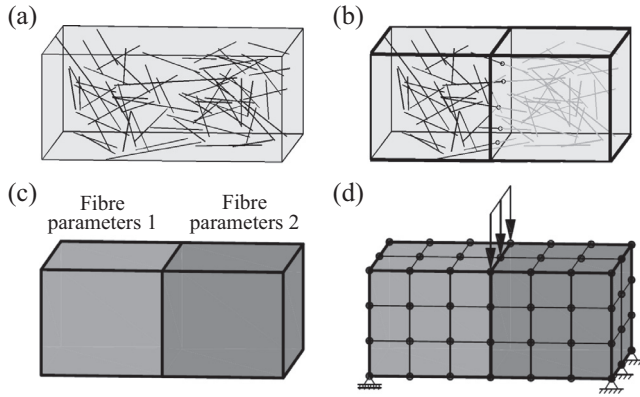


**Fig. 1.** (a) Matrix and fibre structure, (b) discretization in volumes, (c) homogenization within discrete volumes and (d) finite element model.

volume, (iv) defining an adequate constitutive model that describes the behaviour of the FRC at the discrete volume level making use of the fibre structure properties, and finally, (v) simulating the structural response using finite element (FE) modelling.

The constitutive model (iv) is applied at an intermediate level which is between the fibre level and the structural element level. It uses a single-phase material definition, with the consequent computational advantages for application to structural elements. In this way, the definition of the matrix-fibre interface behaviour is circumvented. However, a new issue is raised. As already mentioned, single-phase material models for FRC are commonly calibrated by inverse analysis of test results at the scale of test specimens. Such an approach is not feasible for the intermediate level. Since the focus of this research was on the modelling approach as a whole (i–v) and in the absence of a well-established constitutive modelling technique for this intermediate level, heuristic assumptions were used for the constitutive modelling.

## 2. Modelling approach

Starting from a complete characterization of the fibre structure, this section describes the modelling steps that result in the proposed constitutive model for FRC for use at the discrete volume level. The section ends with an illustration of the constitutive model for various fibre structure parameters.

### 2.1. Fibre parameters within a discrete volume

In the present investigation, fibre structure properties were derived from a complete characterization of the fibre structure in which the precise position of every fibre is known. Several methodologies can be utilized for assessing the fibre structure of an FRC element, including flow simulations [31], numerical algorithms based on probabilistic distributions [26], X-ray Computed Tomography (CT) [20], and visualization of fibres within a viscous transparent fluid [32].

To define the local fibre properties, a discretization of the structural element in volumes was considered. The discrete volume size had to take into account criteria related to the size of the fibres and be sufficiently descriptive of the inhomogeneities of the fibre structure. Fibre properties were determined considering the fibres located in each volume. Because fibres can intersect one or several discrete volumes, the intersection points with the boundaries of the volumes needed to be determined. In this way, each segment of a fibre is considered in the volume in which it is located (Fig. 1b). Intersection points were obtained by assuming that fibres are perfectly straight.

This model incorporates the information from the spatial distribution of the fibres which can potentially influence the mechanical performance of a flowable FRC element, namely the fibre orientation and the local fibre content. The fibre orientation pattern of a body can be described using a set of second-order orientation tensors [23,33–35] defined over a set of discrete volumes of the body. Each orientation tensor describes the fibre orientation state within the volume and can be defined as:

$$\mathbf{A} = \frac{\sum_n L_n \mathbf{p}_n \mathbf{p}_n^T}{\sum_n L_n} \quad (1)$$

where  $\mathbf{A}$  is the orientation tensor of a discrete volume. For all the fibres and fibre segments in the volume,  $\mathbf{p}_n$  is a unit vector in the fibre direction, and  $L_n$  is the length of the fibre or fibre segment. By definition, the orientation tensor has the properties of being symmetric and having normalized components. Symmetric second-order tensors can be visualized using ellipsoids, where the eigenvectors,  $\mathbf{a}_i$ , and eigenvalues,  $\lambda_i$ , give the direction and half-length of the principal axes of the ellipsoids. In this way, ellipsoids are used as a visual tool to identify the dominant direction of the fibres in each discrete volume.

The second aspect, the local fibre content, is expressed in terms of volume fraction ( $v_f$ ) and can be computed for each discrete volume as:

$$v_f = \frac{\sum_n L_n A_f}{V_c} \quad (2)$$

where  $A_f$  is the fibre cross-section area and  $V_c$  the discrete volume. The procedure described here makes it possible to represent the orientation and distribution pattern of a structural element by choosing a certain discretization of the element in volumes and assessing the fibre parameters  $\mathbf{A}$  and  $v_f$  within each discrete volume. This is illustrated in Fig. 2 for the example shown in Fig. 1a.

### 2.2. Definition of fibre efficiency

When a crack arises, the efficiency of a fibre that bridges the crack depends on its orientation with respect to the crack plane. This can be expressed by the angle  $\theta$  between the direction normal to the crack plane ( $\mathbf{n}$ ) and the fibre direction. In a similar manner, it can be assumed that the efficiency of a group of fibres depends on the angle between  $\mathbf{n}$  and the dominant fibre direction of the group of fibres. For the group of fibres (or fibre segments) in each discrete volume, the dominant fibre direction is given by the eigenvector associated with the largest eigenvalue of the orientation tensor ( $\mathbf{a}_1$ ). The angle with respect to the crack plane may therefore be formulated as:

$$\cos \theta = \mathbf{a}_1 \cdot \mathbf{n} \quad (\|\mathbf{a}_1\| = \|\mathbf{n}\| = 1) \quad (3)$$

Fig. 3 depicts two fibre orientation states represented by ellipsoids and illustrates the relevance of the variable  $\cos \theta$  as a measure of fibre efficiency.

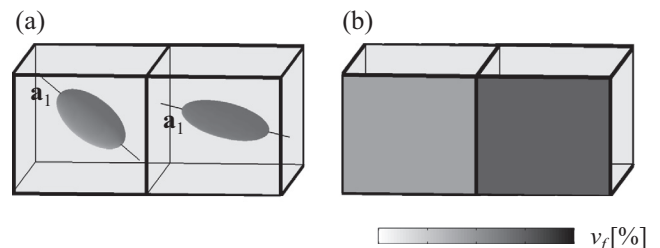


**Fig. 2.** (a) Orientation ellipsoids and dominant fibre orientation and (b) fibre volume fraction.

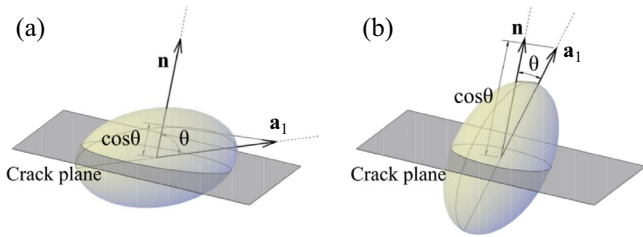


Fig. 3. Orientation state of fibres represented by ellipsoids for (a) a predominantly unfavourable orientation and (b) a favourable orientation.

For convenience, a single variable is introduced that integrates the local fibre orientation with the local volume fraction. This fibre efficiency variable  $\mu$  is defined as a linear combination:

$$\mu = w_1(\cos \theta) + w_2 \left( \frac{v_f}{\bar{v}_f} \right) \quad (4)$$

where  $w_1$  and  $w_2$  are weightings for the orientation and volume fraction components, respectively (with  $w_1 + w_2 = 1$ ), and  $\bar{v}_f$  is the nominal fibre volume fraction of the mix.

It is worth noting that  $\mathbf{a}_1$  and  $v_f$  are material parameters that describe the characteristics of the fibres in each discrete volume of the specimen. In contrast,  $\cos \theta$  and therefore also  $\mu$  are evaluated at each integration point of the FE model, and they are actually variables that depend on the cracking model adopted and the crack plane, so they may change during the simulation. It is worth noting that the FE mesh may not necessarily coincide with the discretization of the fibre structure (as depicted in Fig. 1d).

It should also be mentioned that defining the orientation term in Eq. (3) entails the simplification of the overall orientation state to the direction  $\mathbf{a}_1$ . This aspect is illustrated in Fig. 4, where the orientation tensors of two groups of fibres are visualized using ellipsoids. In Fig. 4a, an elongated ellipsoid represents a markedly unidirectional orientation, while the more spherical ellipsoid in Fig. 4b describes a more isotropic orientation. Both groups have the same dominant direction ( $\mathbf{a}_1$ ), but simplifying the orientation state to  $\mathbf{a}_1$  seems to be adequate only in the first group. This means that the fibre efficiency variable, here defined based on  $\mathbf{a}_1$ , requires a certain degree of unidirectionality of fibres within each discrete volume. This is ensured if the eigenvalues of tensor  $\mathbf{A}$  satisfy the condition that  $\lambda_1$  is significantly greater than  $\lambda_2$  and  $\lambda_3$ .

### 2.3. Uniaxial stress-strain relationship

It is generally agreed that fibres contribute primarily after crack initiation. For this reason, compressive and pre-cracking responses are assumed to agree with those of plain concrete. The uniaxial stress-strain relationship in tension is assumed to be as depicted in Fig. 5, which describes an initial linear-elastic response up to the tensile strength ( $\sigma_1$ ), which characterizes the onset of cracking. After this point, the post-cracking behaviour is described with a tri-linear diagram, as used by several other researchers [4,10,13,14]. The residual tensile strength ( $\sigma_2$ ), which defines an

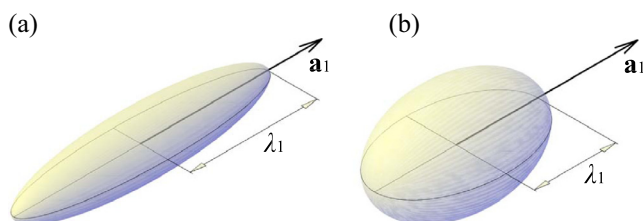


Fig. 4. Orientation state of fibres with equal  $\mathbf{a}_1$  for (a) a markedly unidirectional orientation and (b) an orientation closer to isotropic.

ideal plastic post-cracking behaviour, is defined as dependent on the fibre efficiency variable ( $\mu$ ). When the value of  $\sigma_2$  results in strain softening,  $\sigma_2 < \sigma_1$ , the post-peak drop is assumed to follow the behaviour of plain concrete until it intersects with the residual post-cracking branch, point (2) in Fig. 5a. In contrast, when  $\sigma_2$  exceeds the tensile strength, a hardening response, the residual strength is assumed to be reached at a strain  $\varepsilon_2$  (Fig. 5b). Both plateaus end at a strain level  $\varepsilon_3$ , which activates a softening branch that ends at the ultimate strain  $\varepsilon_{ult}$ . Only the strain levels  $\varepsilon'_2$  and  $\varepsilon_{ult}$ , which are associated with localization of the crack (see Fig. 5), are regularized in terms of the finite element size.

The relationship between the residual tensile strength and the fibre efficiency variable needs to be established based on the type and geometry of the fibres, as well as on the properties of the concrete where the fibres are embedded.

It should be noted that the focus of this paper is on the use of a material model based on actual fibre structure, rather than proposing a more sophisticated description of the stress-strain behaviour for the numerical implementation. With this in mind, it is worth mentioning that the proposed model limits the number of parameters that depend on fibre efficiency to one, namely  $\sigma_2$ , and makes it possible to calibrate the  $\sigma_2$ - $\mu$  relationship against data from standard mechanical characterization tests [16,17]. This is discussed in later sections.

### 2.4. Constitutive modelling

The uniaxial stress-strain behaviour can be generalized to multiaxial stress and strain states by embedding it in a rotating crack model based on a total strain concept, see e.g., Rots [36]. This means that an explicit modelling of the shear retention after cracking is not needed. During an analysis, upon rotation of the principal strains, the (potential) crack orientation rotates and the uniaxial stress-strain behaviour normal to the crack changes too, since it depends on the angle  $\theta$  with the dominant fibre direction.

The dependence of the uniaxial stress-strain relationship on the fibre parameters and on the crack direction is shown in Fig. 6. This figure illustrates an FRC specimen similar to that in Fig. 1a–c. For the sake of clarity, the FE mesh coincides with the volume discretization of the fibre structure in this case. The uniaxial tensile stress-strain relationship at the integration point of each element depends on two main aspects: (1)  $\mathbf{a}_1$  and  $v_f$  as the fibre parameters, and (2) the direction normal to the crack ( $\mathbf{n}$ ), which depends on the current state of stresses. In Fig. 6a, the stress-strain relationships of the two elements differ depending on the dominant fibre direction of each element. Similarly, in Fig. 6b the stress-strain relationships differ based on a variation in the fibre content. Unlike the two previous cases, the two elements in Fig. 6c have the same fibre parameters, but this time different crack directions. Depending on  $\mathbf{n}$ , the variable  $\mu$  and therefore also  $\sigma_2$  are different in each element, which leads once again to two different stress-strain relationships.

This modelling approach is therefore able to take into account both the inhomogeneities of the fibre structure and the dependence of the material on the direction of the principal strains, which is related to the anisotropic behaviour of the material.

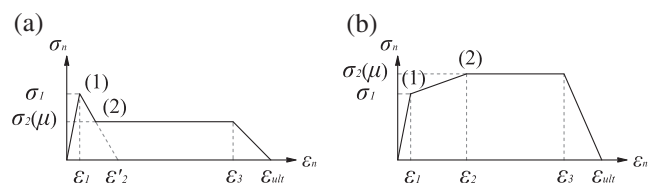


Fig. 5. Uniaxial tensile stress-strain relationship for (a) strain softening and (b) strain hardening behaviour.

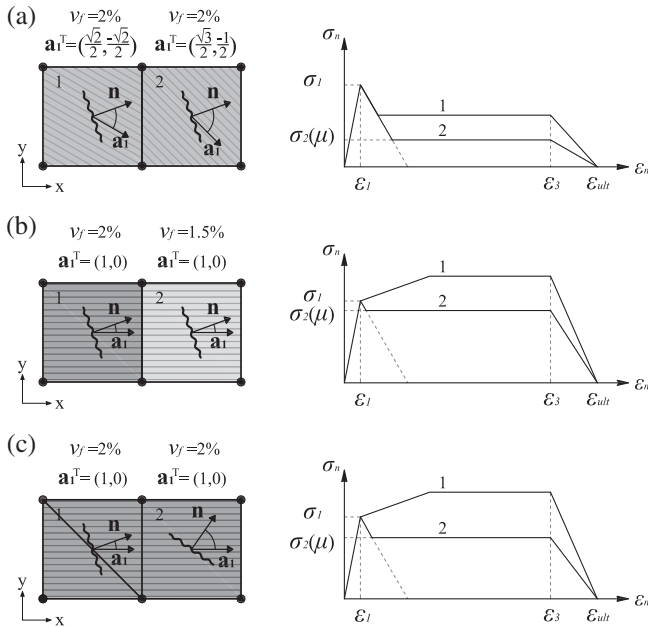


Fig. 6. Tensile constitutive model for two elements with differences in (a) fibre orientation, (b) fibre volume fraction and (c) the direction normal to the crack.

### 3. Two beams in four-point bending tests

The structural performance of a flowable FRC mix with high fibre content was investigated experimentally. In material characterization tests, this mix had previously exhibited high ductility and high residual flexural strength. Two full-scale beams tested in bending showed load-carrying capacity and ductility lower than typically expected and a significant mutual difference in response.

#### 3.1. Materials and specimens

The mix was developed during research work by Kjellmark et al. [37] on the optimization of flowable FRC mixes with high ductility. It has reasonably good casting properties, with adequate flowability and compactability, and it does not require vibration. The mix contains 2 vol% hooked-end steel fibres, with a length of 60 mm and an aspect ratio of 67. Table 1 gives the mix proportions.

The two beams with dimensions of 200 mm × 300 mm × 3000 mm were cast with a falling stream of concrete from a single discharge point, which was initially located at one end of the formwork. When approximately 70% of the formwork was filled, the casting point was moved towards the centre of the formwork to complete the filling. The two beams, FSB-a and FSB-b, were cast with concrete from two different batches, for which the same mixing procedure was adopted.

Table 1  
Mix proportioning.

Component	Dosage
Cement [kg/m <sup>3</sup> ]	492.2
Microsilica [kg/m <sup>3</sup> ]	24.6
Total free water [kg/m <sup>3</sup> ]	197.5
Aggregate 0–8 mm [kg/m <sup>3</sup> ]	1594
Super-plasticizer [kg/m <sup>3</sup> ]	7.38–9.84
Stabilizer [kg/m <sup>3</sup> ]	0.49
Steel fibres [kg/m <sup>3</sup> (vol%)]	156 (2%)
w/b ratio [-]	0.35
Matrix volume (<0.125 mm) [l/m <sup>3</sup> ]	400

Both beams were tested at the age of 28 days under the bending conditions given in Fig. 7. The beams were loaded using a hydraulic jack acting on a steel profile that transferred the load to the loading points. The deflection at mid-span was measured with displacement transducers attached to the bottom face of the beams. For more details on the experimental programme, the reader may refer to Sarmiento et al. [38].

#### 3.2. Experimental results

The crack patterns in Fig. 7 and the load-deflection curves in Fig. 8 show clearly different behaviour in the two beams. In beam FSB-a, several flexural cracks developed, mostly in the central span, after the load reached 50 kN. In the absence of ordinary reinforcement, these cracks were only arrested by the fibres. After cracking, the load applied continued to increase up to 87 kN, when the deflection at midspan was 9.3 mm (deflection-span ratio  $\delta/L$  of 1/280). From this deflection, damage localized in one crack and the load decreased gradually. The critical crack arose within the central span, developed vertically, and merged with multiple

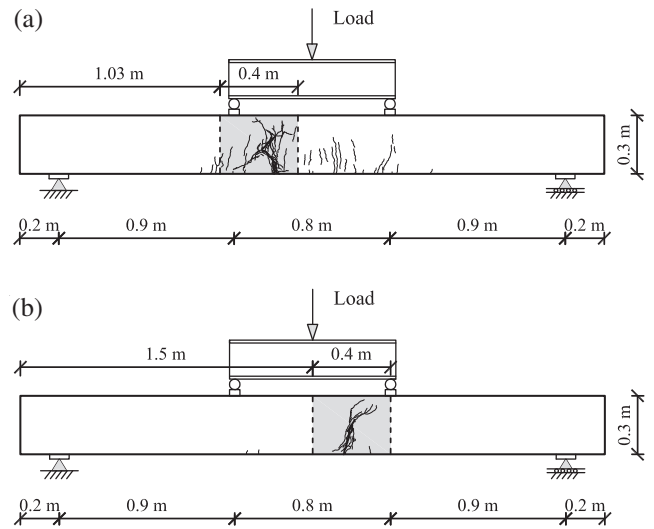


Fig. 7. Experimental setup and final crack pattern of (a) beam FSB-a and (b) beam FSB-b. The shaded parts were sawn and CT-scanned.

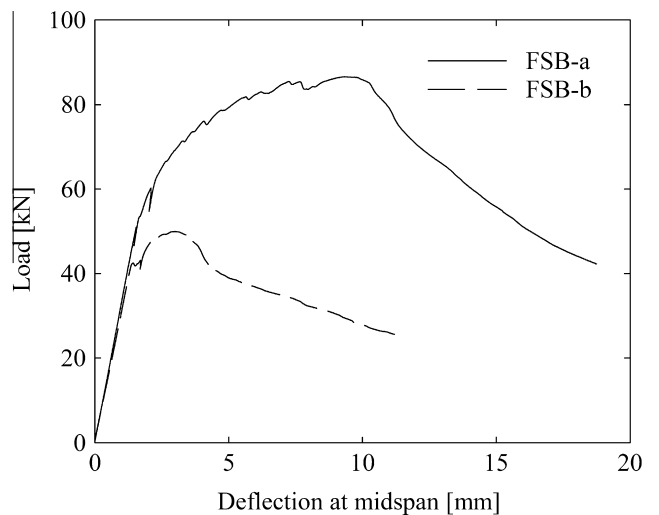


Fig. 8. Experimental load-deflection response of full-scale beams FSB-a and FSB-b.

inclined cracks resulting in diffuse and tortuous paths. During the flexural failure, the beam exhibited some ductility; at a deflection of 17 mm ( $\delta/L \approx 1/150$ ), the beam supported approximately half of its maximum load. Beam FSB-b had a much lower capacity than beam FSB-a. The onset of cracking led to sudden failure along a single crack. This crack started 17 cm from midspan, and propagated at an angle of approximately  $60^\circ$  towards the end of the beam.

#### 4. Modelling and analysis results

The proposed modelling approach was evaluated modelling the beams FSB-a and FSB-b. As a first step to the numerical modelling, the fibre structure had to be obtained and the dependence of the residual strength on the fibre parameters had to be established. Numerical solutions in terms of load-deflection relationships and crack patterns were then compared with the experimental results to validate the approach and determine the predictive ability of the model.

##### 4.1. Fibre structure and fibre parameters

CT scanning has been successfully used as a non-destructive method for the qualitative and quantitative evaluation of the orientation and distribution of steel fibres in FRC [20,35,39,40]. Scanning of an element produces a large number of radiographic images, and digital analysis of the sequence of images allows 3D visualization of the structure of fibres. Moreover, post-processing the images to a skeleton converts fibres into 3D segments located in the volume from which their topology, length and direction can be extracted.

Pieces 400 mm in length containing the critical cracks (Fig. 7) were sawn and examined using a medical CT scanner (Siemens SOMATOM Sensation 4). The fibre skeletons in Fig. 9 provide a first insight into the inhomogeneity of the fibre structure. The figure illustrates the skeleton of fibres in a longitudinal slice just 20 mm thick to avoid too dense an accumulation of fibres in the image.

To locally define  $\mathbf{a}_1$  and  $\nu_f$  from the fibre structure of the sawn pieces, two discretizations in rectangular prismatic volumes were considered. The first discretization comprised  $25 \text{ mm} \times 25 \text{ mm} \times 200 \text{ mm}$  volumes. These volumes anticipated structural analysis with plane stress elements of  $25 \text{ mm} \times 25 \text{ mm}$  and a thickness of 200 mm. The second discretization consisted of  $50 \text{ mm} \times 50 \text{ mm} \times 200 \text{ mm}$  volumes.

Fig. 9 illustrates the sets of orientation ellipsoids and local volume fractions using the fine discretization. The grayscale maps of the volume fractions indicate the presence of areas with low fibre content. Beam FSB-b has a low density of fibres in its upper part, which shows that segregation of fibres has occurred. The orientation ellipsoids look like elongated ellipses in the height-length plane, and the direction of their major axis ( $\mathbf{a}_1$ ) indicates the dominant fibre orientation. The orientation tensors of the 48 discrete volumes of beam FSB-a in Fig. 9a have average ratios of the eigenvalues  $\lambda_2/\lambda_1 = 0.37$  and  $\lambda_3/\lambda_1 = 0.17$ . Note that in isotropic conditions the ratios would satisfy  $\lambda_2/\lambda_1 = \lambda_3/\lambda_1 = 1$  and the orientation ellipsoids would be spheres. This confirms that there is a markedly unidirectional orientation of the fibres within the volumes in the direction  $\mathbf{a}_1$ , which supports the use of the fibre efficiency variable as described in Eq. (3).

##### 4.2. Relationship between the residual tensile strength and fibre efficiency

The relationship between the residual tensile strength ( $\sigma_2$ ) and the fibre efficiency variable ( $\mu$ ) was established from the experi-

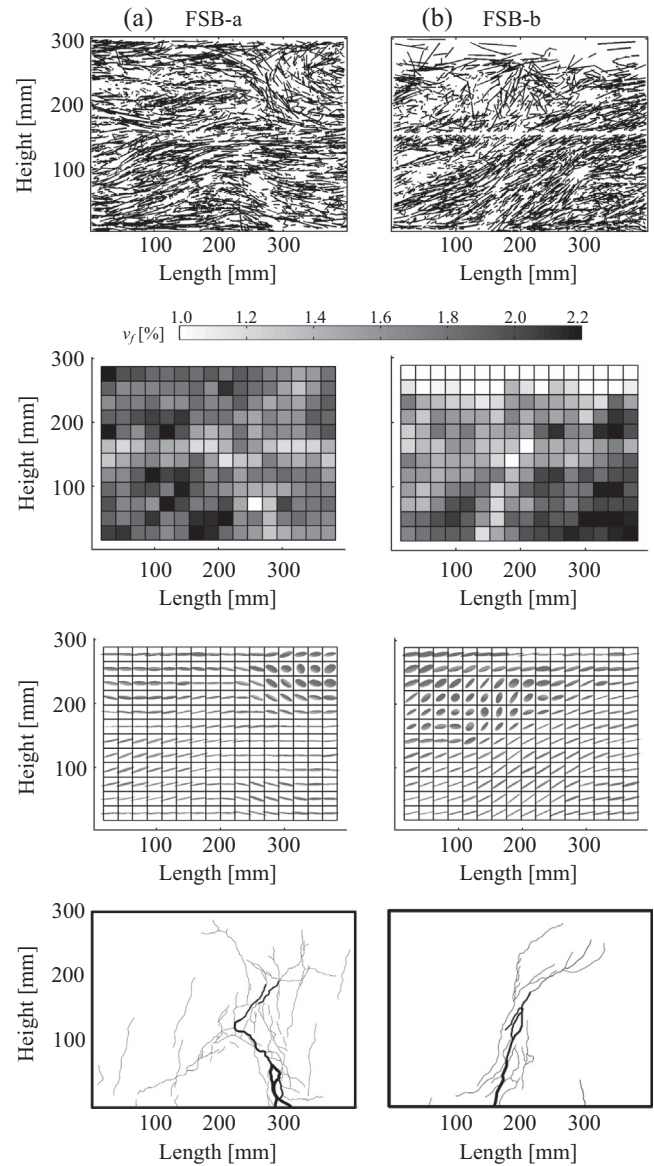


Fig. 9. From top to bottom: skeleton of fibres, local fibre volume fractions, orientation ellipsoids, and crack patterns of the scanned parts of (a) beam FSB-a and (b) beam FSB-b.

mental results of material characterization tests. The set of test specimens consisted of 12 notched beams ( $150 \text{ mm} \times 150 \text{ mm} \times 550 \text{ mm}$ ) and 10 notched cylinders ( $\text{Ø}150 \text{ mm} \times 150 \text{ mm}$ ) that were either cast in moulds or sawn/drilled from a structural element [38]. All the specimens were entirely CT scanned before being tested. The beams were put through three-point bending tests in accordance with EN14651 [1] and the cylinders were tested in uniaxial tension based on RILEM [41].

For the beams, the residual flexural tensile strength corresponding to 2.5 mm crack opening, often denoted  $f_{R3}$ , was used to calibrate the uniaxial residual strength ( $\sigma_2$ ) in accordance with the relationship  $\sigma_2 = f_{R3}/3$ . The principles and assumptions of this relationship can be found elsewhere, e.g., in *fib* [17]. For the cylinders,  $\sigma_2$  was taken as the tensile stress measured at a crack strain value of 0.02. This choice was based on the need to provide a consistent relationship between the results from bending and uniaxial tension tests [42], despite the different strain distribution along the ligament of the respective specimens. Assuming a linear distribution of strains in the beams and the structural characteristic length

equal to the ligament depth (125 mm), a crack width opening of 2.5 mm corresponds to a maximum tensile strain of 0.02 [42]. It is worth mentioning that two of the cylinders did not provide stable measurements at this strain level due to the initially unstable opening of the crack. These two cylinders were therefore excluded from the data set.

To characterize  $\mu$  (Eq. (4)), the fibre parameters  $\mathbf{a}_1$  and  $v_f$  were determined in a slice located in the middle of the specimen with the thickness of the fibre length (60 mm). Because the specimens were notched,  $\mathbf{n}$  was assumed perpendicular to the plane that contained the notched section. Normalized weightings  $w_1$  and  $w_2$  of 0.6 and 0.4, respectively, gave the best curve fit of the data set (see Fig. 10) with the power law:

$$\sigma_2 = 7.7 \mu^{3.5} \quad (\text{in MPa}) \quad (5)$$

The values of  $w_1$  and  $w_2$  highlight the importance of including the variation of the fibre content, and not just the orientation, when defining the post-cracking response of FRC: 60% of the residual strength is explained by variations in the fibre orientation and 40% by variations in the local relative fibre volume fraction. This topic is further discussed in Sarmiento et al. [43].

#### 4.3. Models with inhomogeneous and homogeneous fibre parameters

Due to the geometry and casting conditions of the beams, inhomogeneities of fibres across the width were negligible. In general, the dominant fibre directions  $\mathbf{a}_1$  align parallel to the height-length plane of the beams. For this reason, and without limiting the generality of the foregoing, simulation of the beams FSB-a and FSB-b was addressed as a 2D plane stress problem.

The outline of the model of beam FSB-b is depicted in Fig. 11a. The darker shading corresponds to the scanned region where the fibre parameters were determined. For the rest of the beam, it was assumed that fibres oriented and distributed homogeneously, with  $\mathbf{a}_1$  aligned with the longitudinal direction and fibre content  $v_f = \bar{v}_f$ .

Eight-node quadrilateral plane stress elements were used with  $2 \times 2$  Gauss integration. Two models were defined with the element size ( $l_{el} \times l_{el} \times \text{width of the beam}$ ) coinciding with the volume discretization presented in Section 4.1. Elements with  $l_{el}$  of 25 mm and 50 mm are considered sufficiently fine to allow kinematic modelling of the observed failure patterns and sufficiently coarse to justify a homogenization of the fibre properties within the volumes. A third model combines the coarser discretization of the

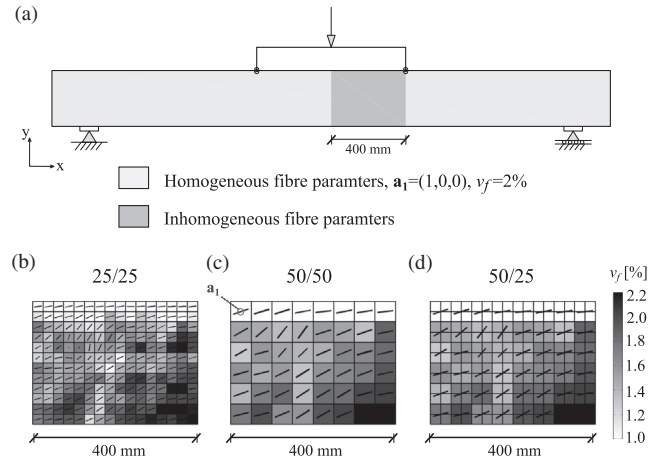


Fig. 11. (a) Outline of the FE model of beam FSB-b. Variations in the fibre orientation and volume fraction that were considered in the elements of models: (b) 25/25, (c) 50/50 and (d) 50/25.

fibre structure with the finer FE mesh. The models are denoted 25/25, 50/50 and 50/25, where the first term refers to the discretization of the fibre structure, and the second term indicates  $l_{el}$  of the finite elements. For example, the fibre parameters assigned to the elements of the inhomogeneous regions of the three models of beam FSB-b are illustrated in Fig. 11b–d. For comparison, models denoted hom/25 and hom/50 were analysed with homogeneous fibre parameters along the entire beam.

The steel profile that distributes the load (Fig. 7) was modelled with beam elements. Incremental loading was applied using deformation control of the centre of the profile. In this way, the external load was transferred symmetrically to the two loading points. The convergence criterion was set at 5% based on a force norm.

#### 4.4. Material parameters for the stress-strain relationship

The material modelling framework presented in Section 2.4 was used. The compressive behaviour was defined using an elastic-ideal plastic model. A compressive strength of 86 MPa was determined experimentally, while the elastic modulus was simply assumed to be 30 GPa. The material parameters that define the stress-strain relationship in tension (Fig. 5) are discussed in the following.

The uniaxial tensile strength  $\sigma_1$  was determined as the average tensile strength of the notched beams and cylinders described in Section 4.2. For the beams tested in bending, the uniaxial strength was estimated from the flexural strength in accordance with the relationship in fib [17]. The strain  $\epsilon'_2$  was defined based on an approximation of the ultimate strain of plain concrete. In smeared cracking, such a strain is considered to be an element-related material property, which is usually estimated from the tensile strength, the fracture energy ( $G_F$ ), and a characteristic length of the element, the equivalent length ( $h$ ). An ultimate strain determined from a linear softening model could underestimate the steepness of the initial softening behaviour, as discussed in Sarmiento et al. [40]. Because the initial part of the softening curve is the most decisive in the current model, it was considered more appropriate to define  $\epsilon'_2$  in accordance with an exponential softening model [44]. In this case,  $\epsilon'_2$  can be expressed as:

$$\epsilon'_2 = \frac{\epsilon_1}{2} + \frac{G_F}{h \sigma_1} \quad (6)$$

Due to the absence of experimental data, the fracture energy was determined in accordance with CEB-FIP [45], and  $h$  was assumed to be  $l_{el}$  (note that all elements are square). The strain  $\epsilon_3$  was calibrated against the experimental results of the cylinders.

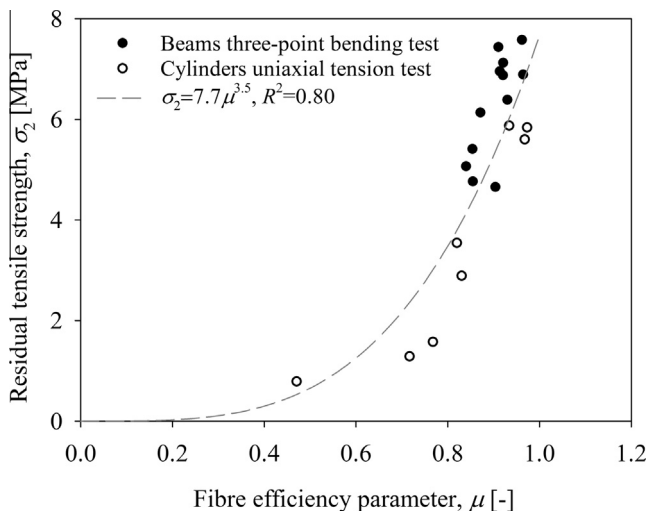


Fig. 10. Relationship between fibre efficiency and residual tensile strength derived from test specimens.

In Fig. 12, the tensile stress is normalized by the residual stress measured at a crack strain of 0.02 (taken as  $\sigma_2$  in Section 4.2) to make it possible to compare the post-cracking responses, which varied greatly depending on the fibre structure. As shown in the figure, the end of the plateau was assumed at a strain  $\epsilon_3$  of 0.1. It is worth noting that the testing machine used to conduct the uniaxial tensile tests was not able to adopt a closed-loop control. Therefore, the test measurements were unstable at the onset of cracking, even for cylinders with a hardening response. This meant that the hardening strain  $\epsilon_2$  at the initiation of the plateau could not be calibrated against the test results. Given that a direct quantification was not possible,  $\epsilon_2$  was estimated to be:

$$\epsilon_2 = \epsilon_1 + 1.5\% \tag{7}$$

In the absence of a well-established formulation, Eq. (7) provides a heuristic approximation of  $\epsilon_2$  in agreement with the values obtained with, for example, *fib* Model Code [17] for the corresponding parameter.

The ultimate strain ( $\epsilon_{ult}$ ) was defined on the basis of the ultimate crack opening ( $w_{ult}$ ) and regularized with the size of the finite element in accordance with  $\epsilon_{ult} = w_{ult}/l_{el}$ . Some investigations, e.g., Kooiman [7] and Cunha [14], have related  $w_{ult}$  to the average projected embedded length of the fibres, which in turn can be determined as  $L_f/4$ , where  $L_f$  is the fibre length. In accordance with this,  $w_{ult} = 15$  mm was used in the present work. Lateral contraction effects were neglected because the material was extensively cracked from an early stage of the analysis. The material parameters for this example are summarized in Table 2.

4.5. Analysis results and discussion

Fig. 13a and b compare the experimental load-displacement curves of the beams FSB-a and FSB-b with their respective numerical solutions. The markers indicate the points where the analyses failed to reach full convergence. Non-converged steps were always alternated with converged steps: within any deflection interval of 1.6 mm, at least one step converged.

As expected, all the models predict exactly the same load-deflection relationship up to the onset of cracking. From that point on, the response depends greatly on the model. The homogeneous fibre models provide a large load increase associated with strain hardening of the tensile stress-strain relationship. Note that for the homogeneous fibre parameters ( $\mathbf{a}_1 = (1,0,0)$  and  $\nu_f = 2\%$ ) and a vertical crack plane ( $\mathbf{n} = (1,0,0)$ ), the residual strength  $\sigma_2$  in Eq. (5) takes the value 7.7 MPa. This value represents a theoretical case and is not intended to correspond to the results of standard beams, for which the average residual strength was somewhat lower (6.3 MPa). A change of slope in the load-deflection curves of the hom/25 and hom/50 models occurs when the strains in the central span reach the plateau of the  $\sigma_n-\epsilon_n$  diagram. Beyond this point, the load increases due to the spread of the fracture area, which activates an increasing number of fibres.

There are large differences in the load-deflection curves between homogeneous and inhomogeneous models, especially for beam FSB-b, whose fibre properties were particularly unfavourable. Apart from this, the three inhomogeneous models are able to predict the different structural performance between the two

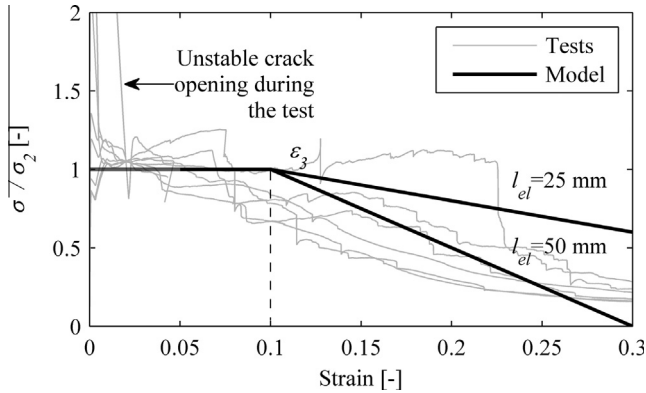


Fig. 12. Calibration of the material parameter  $\epsilon_3$  against the experimental uniaxial tension tests of cylinders.

Table 2  
Material input parameters.

Component	
Young modulus [MPa]	30,000
Poisson ratio [-]	0
Compressive strength [MPa]	86
Fracture energy plain concrete, $G_f$ [N/mm]	0.113
Tensile strength, $\sigma_1$ [MPa]	5.12
$\epsilon_1$ [-]	$1.71 \cdot 10^{-4}$
$\epsilon_2'$ [-] for $l_{el} = 25$ mm/50 mm	$9.67 \cdot 10^{-4}/5.26 \cdot 10^{-4}$
$\epsilon_2$ [-]	$1.67 \cdot 10^{-3}$
$\epsilon_3$ [-]	0.10
$\epsilon_{ult}$ [-] for $l_{el} = 25$ mm/50 mm	0.60/0.30

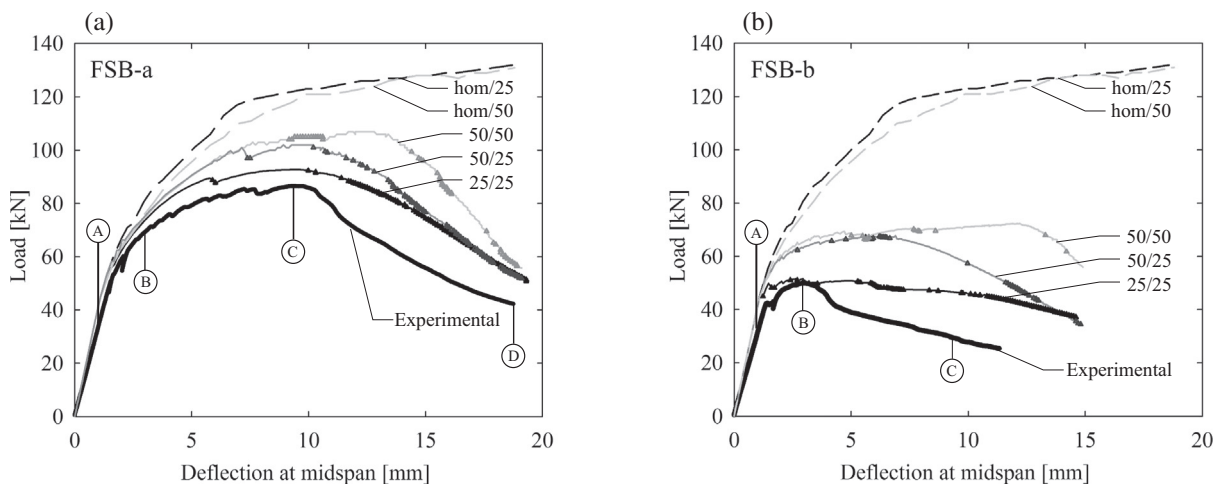


Fig. 13. Experimental and modelled load-deflection responses of full-scale beams: (a) FSB-a and (b) FSB-b.

beams just by considering the fibre parameters in the inhomogeneous region. Nevertheless, the 50/50 and 50/25 models significantly overestimate the experimental results. Only the 25/25 model offers a realistic prediction up to the peak load; although it still overestimates the post-peak response.

Fig. 14 illustrates the crack propagation phenomenon with the 25/25 model. The contour plots depict the maximum principal strain at various deflection stages (A, B, C and D in Fig. 13). At stage A, cracking has initiated in the lower part of the beams. With increasing load, the crack localizes in the inhomogeneous region. In beam FSB-a, an inclined crack develops at the same time as the damage zone grows (see stage B in Fig. 14a). At stage C, cracking has spread over the inclined crack and in the lower part of the central span. The highly deformed areas sustain a constant stress, because the strains range within the limits of the plateau of the  $\sigma_n$ - $\epsilon_n$  diagram. Globally, the beam has reached the maximum load. Increasing the load causes crack localization in the inhomogeneous region once again. The load decreases gradually due to the unloading of the adjacent regions and the strain softening of the critical crack when reaching the strain level  $\epsilon_3$ . Stage D shows the critical crack around a densely fractured area.

The critical crack of beam FSB-b develops at the onset of cracking (Fig. 14b). At stage B, the beam has reached the maximum load, and the critical crack has developed beyond 80% of the height of the beam. Increasing load leads to propagation of the crack towards the compressive zone. The crack path bifurcates in two opposite horizontal directions (see stage C). This splitting crack is the result of the large reduction in the compressive zone depth above the crack, causing transverse tensile stresses. The crack easily propagates horizontally due to the low residual tensile strength in the vertical direction. This is related to the lack of fibres aligned in this direction and the low fibre content in the upper part of the beam. From a numerical point of view, the bifurcating crack path can also be due to the complex stress fields at the tips of the cracks paths [46,47]. Experimentally, the crack branched and inclined close to this area, but only in the direction of the end of the beam.

In general, the 25/25 model accurately predicts the location of the critical crack. Limiting the fibre inhomogeneity to a part of

the model undoubtedly helped localize the crack in this region, but besides the crack location the model is able to capture adequately its propagation and the overall fracture process as well.

Comparison of the load-deflection results of the 50/25 and 25/25 models provides actual information on the extent to which the inhomogeneity of the fibre structure is well captured. The two models correlate closely only at large deflections. Otherwise, the 50/25 model estimates a greater post-cracking response and peak load. This can be ascribed to variations in the residual strength  $\sigma_2$  caused by homogenizing the fibre parameters in smaller or larger volume regions. If larger volumes are used, possible weak paths are “averaged away” (see Fig. 11b and d), which explains why the load-carrying capacity of the 50/25 model is greater than that of the 25/25 model.

Up to its peak load, the results of the 50/25 model agree with those of the 50/50 model. The 50/50 model, however, reaches its peak load at a considerably greater deflection. Since the load decreases when the maximum strain exceeds  $\epsilon_3$ , it seems that this strain level may not have been properly calibrated. This parameter needs further study, especially in terms of its mesh-size dependence.

Fig. 15 illustrates the strain contours of the three models of beam FSB-b at the deflection stage B. Only the inhomogeneous

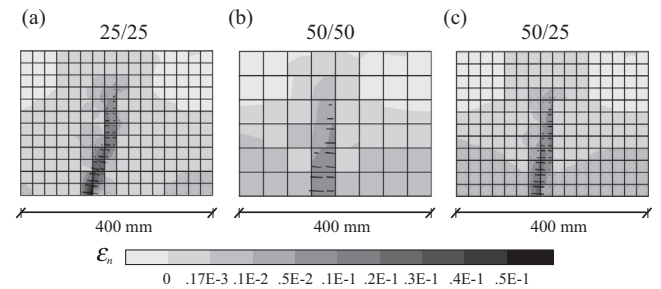


Fig. 15. Strain levels of the maximum principal strain and vectors for the inhomogeneous region of beam FSB-b in the three models: (a) 25/25, (b) 50/50 and (c) 50/25.

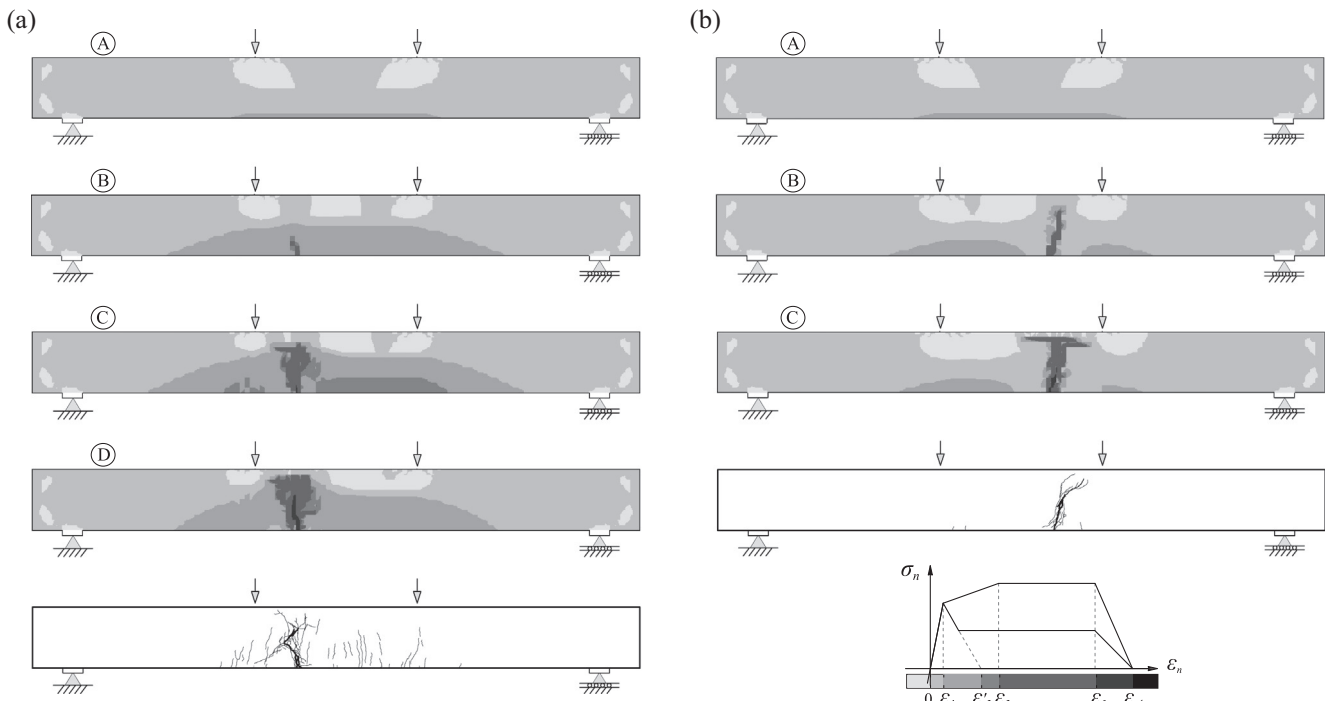


Fig. 14. Strain levels of the maximum principal strain for beams: (a) FSB-a and (b) FSB-b. The deflection levels A, B, C and D are depicted in Fig. 13.

region is depicted. The 25/25 model shows the highly concentrated strains that follow the weak path of the fibre parameters (Fig. 11a). In the 50/25 and 50/50 models, the location of the critical crack is slightly offset because of the greater homogenization of the fibre structure in coarser volumes. Nevertheless, both models capture a certain inclination of the crack.

## 5. Summary and conclusions

The current paper presents a modelling approach for FRC structural elements in which the fibre structure is considered at an intermediate level between the fibre level and the structural element level. The fibre structure is discretized and homogenized in volumes, and incorporated in a numerical model. The model uses a single-phase material definition depending on the local fibre parameters. In the absence of well-established constitutive modelling techniques for this intermediate level, a simplified stress-strain relationship was adopted. Heuristic material parameters were assumed, and a phenomenological relationship to describe the effect of the fibre parameters in the post-cracking response was calibrated. Further refinements should be aimed at establishing a fundamentally-based definition of the material at this level to make it possible to generalize the use of the method.

The modelling approach was implemented to analyse two beams in bending tests. The fibre structures of the beams in their critical region were obtained using CT scanning. The numerical results of the models incorporating these actual fibre structures presented large differences from the models assuming homogeneous fibre properties. The approach was able to capture a large difference in the bending capacity of the two beams, which can only be attributed to the differences in their fibre structures. Furthermore, it provided an adequate prediction of the location and propagation of the critical cracks. The estimated maximum load proved to be sensitive to the volume discretization of the fibre structure. A discretization in the range of half the fibre length led to a good agreement with the experimental maximum loads. In general, the post-peak responses were somewhat overestimated, which might be expected in view of the simplicity of the material model.

The use of this numerical approach is especially relevant to structural elements in which the flow of FRC at the casting stage is expected to lead to an uneven distribution of the fibres. The approach can be applied to structural elements whose fibre structure is obtained using flow simulations. Furthermore, the low computational cost of the numerical analyses makes it possible to study more complex structures.

## Acknowledgements

The authors wish to acknowledge support from COIN – the Concrete Innovation Centre ([www.coinweb.no](http://www.coinweb.no)) – a centre for research-based innovation, which was initiated by the Research Council of Norway (RCN) in 2006 for an eight-year period. The Centre was directed by SINTEF, with NTNU as a research partner, and the most recent industrial partners included Aker Solutions, Norcem, Norwegian Public Roads Administration, Rescon Mapei, Skanska, Unicon, Veidekke, and Weber Saint Gobain.

## References

- [1] European Standard. EN 14651:2005. Test method for metallic fibre concrete – measuring the flexural tensile strength (limit of proportionality (LOP), residual). Brussels, Belgium: European Committee for Standardization; 2005.
- [2] ASTM International. ASTM C1550-12a, Standard test method for flexural toughness of fiber reinforced concrete (using centrally loaded round panel). West Conshohocken, PA, USA; 2012.
- [3] Ozyurt N, Mason TO, Shah SP. Correlation of fiber dispersion, rheology and mechanical performance of FRCs. *Cem Concr Compos* 2007;29(2):70–9.
- [4] Löfgren I, Stang H, Olesen JF. The WST method, a fracture mechanics test method for FRC. *Mater Struct* 2008;41:197–211.
- [5] Di Prisco M, Ferrara L, Lamperti MGL. Double edge wedge splitting (DEWS): an indirect tension test to identify post-cracking behaviour of fibre reinforced cementitious composites. *Mater Struct* 2013;46:1893–918.
- [6] Uchida Y, Kurihara N, Rokugo K, Koyanagi W. Determination of tension softening diagrams of various kinds of concrete by means of numerical analysis. In: Wittmann FH, editor. Proceedings of fracture mechanics of concrete structures (FRAMCOS-2). Freiburg, Germany: Aedificatio; 1995.
- [7] Kooiman AG. Modelling steel fibre reinforced concrete for structural design [Doctoral thesis]. Rotterdam: Delft University of Technology; 2000.
- [8] Grünwald S. Performance based design of self compacting steel fiber reinforced concrete [Doctoral thesis]. Rotterdam: Delft University of Technology; 2004.
- [9] Meda A, Plizzari GA, Sorelli L. Uni-axial and bending test for the determination of fracture properties of fiber reinforced concrete. In: Li VC, Leung CKY, Willam KJ, Billington SL, editors. Proceedings of the fifth international conference on fracture mechanics of concrete and concrete structures, vol. 2, 2004. p. 1163–70.
- [10] Barros JAO, Cunha VMCF, Ribeiro AF, Antunes JAB. Post-cracking behaviour of steel fibre reinforced concrete. *Mater Struct* 2005;38:47–56.
- [11] De Oliveira e Sousa J, Gettu R. Determining the tensile stress-crack opening curve of concrete by inverse analysis. *J Eng Mech* 2006;132(2):141–8.
- [12] Tlemat H, Pilakoutas K, Neocleous K. Modelling of SFRC using inverse finite element analysis. *Mater Struct* 2006;39:221–33.
- [13] Cominoli L, Meda A, Plizzari GA. Fracture properties of high-strength hybrid fiber-reinforced concrete. In: Grosse CU, editor. Advances in construction materials 2007. Berlin Heidelberg: Springer; 2007. p. 139–46.
- [14] Cunha VMCF. Steel fibre reinforced self-compacting concrete (from micromechanics to composite behavior) [Doctoral thesis]. Braga, Portugal: Universidade do Minho; 2010.
- [15] RILEM. RILEM TC162-TDF: test and design methods for steel fibre reinforced concrete. Design of steel fibre reinforced concrete using the  $\sigma$ -w method: principles and applications. *Mater Struct* 2002;35:262–78.
- [16] RILEM. RILEM TC162-TDF: test and design methods for steel fibre reinforced concrete.  $\sigma$ - $\epsilon$ -design method – final recommendation. *Mater Struct* 2003;36:560–7.
- [17] *fib*. Model Code for Concrete Structures 2010, International Federation for Structural Concrete (*fib*); 2010.
- [18] DAFStb. Steel fibre reinforced concrete. Berlin, Germany: DAFStb (German Committee for Structural Concrete); 2012.
- [19] Ferrara L, Meda A. Relationships between fibre distribution, workability and the mechanical properties of SFRC applied to precast roof elements. *Mater Struct* 2006;39:411–20.
- [20] Stähli P, Custer R, van Mier JGM. On flow properties, fibre distribution, fibre orientation and flexural behaviour of FRC. *Mater Struct* 2008;41:189–96.
- [21] Vandewalle L, Heirman G, van Rickstal F. Fibre orientation in self-compacting fibre reinforced concrete. In: Tanikella PND, Gettu R, editors. On the distribution of fibers in self compacting concrete. Proc of the 7th int RILEM symp on fibre reinforced concrete: design and applications (BEFIB2008). Chennai, India: RILEM Publications SARL; 2008. p. 719–28.
- [22] Boulekache B, Hamrat M, Chemrouk M, Amziane S. Flowability of fibre-reinforced concrete and its effect on the mechanical properties of the material. *Constr Build Mater* 2010;24(9):1664–71.
- [23] Ferrara L, Ozyurt N, di Prisco M. High mechanical performance of fibre reinforced cementitious composites: the role of “casting-flow induced” fibre orientation. *Mater Struct* 2011;44:109–28.
- [24] Abrishambaf A, Barros JAO, Cunha VMCF. Relation between fibre distribution and post-cracking behaviour in steel fibre reinforced self-compacting concrete panels. *Cem Concr Res* 2013;51:57–66.
- [25] Radtke FKF. Computational modelling of fibre-reinforced cementitious composites: an analysis of discrete and mesh-independent techniques [Doctoral thesis]. Rotterdam: Delft University of Technology; 2012.
- [26] Cunha VMCF, Barros JAO, Sena-Cruz JM. A finite element model with discrete embedded elements for fibre reinforced composites. *Comput Struct* 2012;94:95:22–33.
- [27] Huespe AE, Oliver J, Mora DF. Computational modeling of high performance steel fiber reinforced concrete using a micromorphic approach. *Comput Mech* 2013;52(6):1243–64.
- [28] Laranjeira de Oliveira F. Design-oriented constitutive model for steel fibre reinforced concrete [Doctoral thesis]. Barcelona, Spain: Universitat Politècnica de Catalunya; 2010.
- [29] Cunha V, Barros J, Sena-Cruz J. Pullout behavior of steel fibers in self-compacting concrete. *J Mater Civ Eng* 2010;22(1):1–9.
- [30] Sandbakk S. Fibre reinforced concrete. Evaluation of test methods and material development [Doctoral thesis]. Trondheim, Norway: Norwegian University of Science and Technology; 2011.
- [31] Švec O, Škočej J, Stang H, Olesen JF, Poulsen PN. Flow simulation of fiber reinforced self compacting concrete using Lattice Boltzmann method. In: 13th International congress on the chemistry of cement (ICC), Madrid, Spain, 2011.
- [32] Zhou B, Uchida Y. Fiber orientation in ultra high performance fiber reinforced concrete and its visualization. In: Van Mier JGM, Ruiz G, Andrade C, Yu RC, Zhang XX, editors. VIII international conference on fracture mechanics of concrete and concrete structures (FraMCoS-8). Toledo, Spain: International Center for Numerical Methods in Engineering; 2013.

- [33] Advani SG, Tucker CL. The use of tensors to describe and predict fiber orientation in short fiber composites. *J Rheol* 1987;31(8):751–84.
- [34] Şanal İ, Özyurt Zihnioglu N. To what extent does the fiber orientation affect mechanical performance? *Constr Build Mater* 2013;44:671–81.
- [35] Švec O, Žirgulis G, Bolander JE, Stang H. Influence of formwork surface on the orientation of steel fibres within self-compacting concrete and on the mechanical properties of cast structural elements. *Cem Concr Compos* 2014;50:60–72.
- [36] Rots JG. Computational modeling of concrete fracture [Doctoral thesis]. Rotterdam: Delft University of Technology; 1988.
- [37] Kjellmark G, Martius-Hammer TA, Kanstad T. COIN's 15 MPa target fibre concrete: materials development towards high residual flexural strength. In: Proceedings of the XXII Nordic concrete research symposium. Reykjavik, Iceland: Norsk Betongforening; 2014. p. 215–8.
- [38] Sarmiento EV, Geiker MR, Kanstad T. Influence of fibre configuration on the mechanical behaviour of standard test specimens and full-scale beams made of flowable FRC. *Constr Build Mater* 2016;111:794–804.
- [39] Suuronen J-P, Kallonen A, Eik M, Puttonen J, Serimaa R, Herrmann H. Analysis of short fibres orientation in steel fibre-reinforced concrete (SFRC) by X-ray tomography. *J Mater Sci* 2013;48(3):1358–67.
- [40] Sarmiento EV, Hendriks MAN, Kanstad T. Accounting for the fibre orientation on the structural performance of flowable fibre reinforced concrete. In: Bicanic N, Mang H, Meschke G, de Borst R, editors. Computational modelling of concrete structures. CRC Press; 2014. p. 609–18.
- [41] RILEM. RILEM TC 162-TDF: test and design methods for steel fibre reinforced concrete. Uni-axial tension test for steel fibre reinforced concrete – recommendations. *Mater Struct* 2001;34:3–6.
- [42] Ferrara L, Caverzan A, Muhaxheri M, di Prisco M. Identification of tensile behaviour of SFR-SCC: direct vs. indirect tests. In: Barros J, editor. BEFIB2012 – fibre reinforced concrete, vol. 1. RILEM Publications SARL; 2012. p. 189–200.
- [43] Sarmiento EV, Kanstad T, Geiker MR, Hendriks MAN. Impact of the combined effect of fibre orientation and volume fraction on the mechanical properties of fibre reinforced concrete. In: Proceedings of the XXII Nordic concrete research symposium. Reykjavik, Iceland: Norsk betongforening; 2014. p. 141–4.
- [44] TNO DIANA. Material library. In: Manie J, Kikstra WP, editors. DIANA finite element analysis user's manual, release 9.6. Delft, The Netherlands: TNO DIANA; 2014.
- [45] CEB-FIP. Model code for concrete structures 1990. Lausanne, Switzerland: Comité Euro-International du Béton; 1990.
- [46] Jirásek M, Bauer M. Numerical aspects of the crack band approach. *Comput Struct* 2012;110–111:60–78.
- [47] Slobbe AT, Hendriks MAN, Rots JG. Smoothing the propagation of smeared cracks. *Eng Fract Mech* 2014;132:147–68.